applied sciences

MDPI

Article

Segregation of $NiTe_2$ and $NbTe_2$ in *p*-Type Thermoelectric $Bi_{0.5}Sb_{1.5}Te_3$ Alloys for Carrier Energy Filtering Effect by Melt Spinning

Hyun-Sik Kim [1,†], TaeWan Kim [2,†], Jiwoo An [3], Dongho Kim [3], Ji Hoon Jeon [3] and Sang-il Kim [3,*]

1 Department of Materials Science and Engineering, Hongik University, Seoul 04066, Korea; hyunsik.kim@hongik.ac.kr
2 Department of Electrical Engineering and Smart Grid Research Center, Jeonbuk National University, Jeonju 54896, Korea; twkim@jbnu.ac.kr
3 Department of Materials Science and Engineering, University of Seoul, Seoul 02504, Korea; ajwoo8020@uos.ac.kr (J.A.); hoo829@uos.ac.kr (D.K.); wlgns10123@uos.ac.kr (J.H.J.)
* Correspondence: sang1.kim@uos.ac.kr
† These authors contributed equally to this work.

Abstract: The formation of secondary phases of $NiTe_2$ and $NbTe_2$ in *p*-type $Bi_{0.5}Sb_{1.5}Te_3$ thermoelectric alloys was investigated through in situ phase separation by using the melt spinning process. Adding stoichiometric Ni, Nb, and Te in a solid-state synthesis process of $Bi_{0.5}Sb_{1.5}Te_3$, followed by rapid solidification by melt spinning, successfully segregated $NiTe_2$ and $NbTe_2$ in the $Bi_{0.5}Sb_{1.5}Te_3$ matrix. Since heterointerfaces of $Bi_{0.5}Sb_{1.5}Te_3$ with $NiTe_2$ and $NbTe_2$ form potential barriers of 0.26 and 0.08 eV, respectively, a low energy carrier filtering effect can be expected; higher Seebeck coefficients and power factors were achieved for $Bi_{0.5}Sb_{1.5}Te_3(NiTe_2)_{0.01}$ (250 μV/K and 3.15 mW/mK^2), compared to those of $Bi_{0.5}Sb_{1.5}Te_3$ (240 μV/K and 2.69 mW/mK^2). However, there was no power factor increase for $NbTe_2$ segregated samples. The decrease in thermal conductivity was seen due to the possible additional phonon scattering by the phase segregations. Consequently, zT at room temperature was enhanced to 0.98 and 0.94 for $Bi_{0.5}Sb_{1.5}Te_3(NiTe_2)_{0.01}$ and $Bi_{0.5}Sb_{1.5}Te_3(NbTe_2)_{0.01}$, respectively, compared to 0.79 for $Bi_{0.5}Sb_{1.5}Te_3$. The carrier filtering effect induced by $NiTe_2$ segregations with an interface potential barrier of 0.26 eV effectively increased the Seebeck coefficient and power factor, thus improving the zT of *p*-type $Bi_{0.5}Sb_{1.5}Te_3$, while the interface potential barrier of 0.08 eV of $NbTe_2$ segregation appeared to be too small to induce an effective carrier filtering effect.

Keywords: $Bi_{0.5}Sb_{1.5}Te_3$; heterointerface; phase separation; carrier energy filtering; secondary phase

check for updates

Citation: Kim, H.-S.; Kim, T.; An, J.; Kim, D.; Jeon, J.H.; Kim, S.-i. Segregation of $NiTe_2$ and $NbTe_2$ in *p*-Type Thermoelectric $Bi_{0.5}Sb_{1.5}Te_3$ Alloys for Carrier Energy Filtering Effect by Melt Spinning. *Appl. Sci.* **2021**, *11*, 910. https://doi.org/10.3390/app11030910

Received: 7 December 2020
Accepted: 18 January 2021
Published: 20 January 2021

Publisher's Note: MDPI stays neutral with regard to jurisdictional claims in published maps and institutional affiliations.

Copyright: © 2021 by the authors. Licensee MDPI, Basel, Switzerland. This article is an open access article distributed under the terms and conditions of the Creative Commons Attribution (CC BY) license (https://creativecommons.org/licenses/by/4.0/).

1. Introduction

Research on renewable energy generation has attracted considerable attention because traditional energy resources have become more limited. In addition, approximately 60% of the total energy is lost as waste heat during energy generation and consumption. Therefore, thermoelectric power generation has several advantages as a power generation technology to use energy more efficiently [1,2]. Thermoelectric materials can directly convert the temperature gradient into electrical energy, and they have attracted considerable attention in recent decades. In particular, bismuth telluride (Bi_2Te_3)-based alloys exhibit high thermoelectric performance at near-room temperature [1,2]. They can be applied either to power generation from low grade waste heat, or in thermoelectric solid-state cooling to replace traditional refrigeration [1,2]. The thermoelectric efficiency is determined in terms of a thermoelectric dimensionless figure of merit, expressed as $zT = \sigma \cdot S^2 \cdot T/\kappa$, where σ is the electrical conductivity, S is the Seebeck coefficient, T is the absolute temperature, and κ is the thermal conductivity [3].

Many approaches have been adopted to enhance the zT of thermoelectric materials. To improve electrical transport properties, approaches such as band convergence, carrier

energy filtering, and resonance doping have been applied [4–6]. In addition, a variety of defect structures is introduced to the material to reduce the κ by intensifying phonon scattering [7–9]. For example, nanograin-composite, dense dislocations formed at the grain boundary, and substitutional doping have been known as effective approaches to reduce κ by intensifying phonon scattering in (Bi_2Te_3)-based alloys [8–12]. Among these approaches, introducing nanoparticles in the thermoelectric materials can improve zT by increasing the electrical transport properties and reduction in κ. The reduction in κ can be attained by additional phonon scattering by the embedded nanoparticles [13], and the increase in the electrical transport properties can be attributed to the carrier energy filtering effect caused by the nanoparticles. The carrier filtering effect is a strong energy dependence of the carrier relaxation time caused by band bending at the interface between metallic inclusions and thermoelectric materials [14–16].

In this study, the formation of secondary phases of $NiTe_2$ and $NbTe_2$ in *p*-type $Bi_{0.5}Sb_{1.5}Te_3$ thermoelectric alloys related with the carrier filtering effect was investigated through in situ phase segregation by using the melt spinning process. Metallic $NiTe_2$ and $NbTe_2$ were chosen for the successful segregation in $Bi_{0.5}Sb_{1.5}Te_3$ alloys, using the melt spinning process, which was observed in the preliminary experiment. Adding excess stoichiometric composition of $NiTe_2$ and $NbTe_2$ in the melt-process of $Bi_{0.5}Sb_{1.5}Te_3$ synthesis successfully segregated $NiTe_2$ and $NbTe_2$ phases through the rapid solidification process by melt spinning. As heterointerfaces of semiconducting $Bi_{0.5}Sb_{1.5}Te_3$ with metallic $NiTe_2$ and $NbTe_2$, a possible carrier energy filtering effect can be expected. In addition, the segregation of $NiTe_2$ and $NbTe_2$ would intensify the phonon scattering, possibly reducing κ.

2. Materials and Methods

Ingots of $Bi_{0.5}Sb_{1.5}Te_3(NiTe_2)_x$ (x = 0, 0.003, 0.01, 0.1) and $Bi_{0.5}Sb_{1.5}Te_3(NbTe_2)_x$ (x = 0, 0.005, 0.01, 0.1) were prepared by conventional melting and quenching techniques using high-purity elemental Bi (99.999%, shots, 5N Plus, Montreal, QC, Canada), Sb (99.999%, shots, 5N Plus), Te (99.999%, pieces, 5N Plus), Nb (99.99%, powder, Sigma Aldrich, St. Louis, MO, USA), and Ni (99.9%, powder, Sigma Aldrich), as starting materials. Stoichiometric mixtures were loaded into a quartz tube (15 mm in diameter). The tube was vacuum-sealed under 10^{-4} torr, and the contents were melted in a box furnace at 1423 K for 20 h, and then quenched to room temperature. The ingots were grounded using a high-energy ball mill (8000D, SPEX, Metuchen, NJ, USA) for 5 min. Subsequently, melt spinning of the prepared ingots (except for $Bi_{0.5}Sb_{1.5}Te_3(NiTe_2)_{0.1}$ and $Bi_{0.5}Sb_{1.5}Te_3(NbTe_2)_{0.1}$) was performed, under a copper wheel rotation of 3600 rpm, and the molten solution was shot at 0.03 MPa under Ar. The ribbons were grounded in an agate mortar. Then, disk-shaped polycrystalline bulk samples (10 mm in diameter and 10 mm thickness) were prepared by spark plasma sintering (SPS) at 430 °C for 5 min, under 50 MPa in vacuum.

X-ray diffraction (XRD, D8 Discover, Bruker, Billerica, MA, USA) was performed for phase analysis. The temperature-dependent S and σ parameters were measured within a temperature range from room temperature to 480 K on the samples, perpendicular to the direction of the applied pressure (ZEM-3 Advanced-RIKO, Yokohama, Japan). The nominal temperature gradients were given as 10, 20, and 30 K. The experimental error margin for S and σ are estimated as ±5% and ±3%, respectively. The carrier concentrations were determined by van der Pauw measurements under a magnetic field of 0.5 T (AHT-55T5, Ecopia, Anyang, Korea) in the same direction; the input current can be regulated between 1 nA and 20 mA. The van der Pauw method typically provides the carrier concentration with relative error within 5%. The κ values of the samples were calculated from the expression $\kappa = \rho_s \cdot C_p \cdot \lambda$, considering their theoretical density (ρ_s), heat capacity (C_p), and thermal diffusivity (λ) measured across the same direction (perpendicular to the pressing direction), so the zT can be determined. The C_p values from 300 K to 400 K were measured by using a physical property measurement system (PPMS, Quantum Design, San Diego, CA, USA), and 121.6 J mol^{-1} K^{-1} were used, which were estimated from Dulong–Petit fitting. The densities of all samples were measured as being higher than 98.5%, from

the sintered samples of cylinder shape and 10 mm diameter with ~12 mm height, by the Archimedes method, and the ρ_s for $Bi_{0.5}Sb_{1.5}Te_3$ of 6.88 g/cm^3 was used for samples with small addition ($x \leq 0.01$). The λ were measured using a laser flash installation (Laser Flash Analysis, LFA 467, Netzsch, Selb, Germany). The experimental error margin for λ is estimated as $\pm$3%.

3. Results

Figure 1a,b shows XRD patterns of the melt-spun ribbons of $Bi_{0.5}Sb_{1.5}Te_3(NiTe_2)_x$ (x = 0.1) and $Bi_{0.5}Sb_{1.5}Te_3(NbTe_2)_x$ (x = 0.1). Figure 1c,d shows XRD patterns of the SPS-sintered samples of $Bi_{0.5}Sb_{1.5}Te_3(NiTe_2)_x$ (x = 0, 0.003, 0.01, and 0.1) and $Bi_{0.5}Sb_{1.5}Te_3(NbTe_2)_x$ (x = 0, 0.005, 0.01, and 0.1). For all samples, the diffraction peaks of the major phase were related to the $Bi_{0.5}Sb_{1.5}Te_3$ structure (JCPDS #00-49-1713). The XRD patterns of $Bi_{0.5}Sb_{1.5}Te_3(NiTe_2)_{0.1}$ and $Bi_{0.5}Sb_{1.5}Te_3(NbTe_2)_{0.1}$ with x = 0.1 showed additional peaks of the segregated phases of $NiTe_2$ (JCPDS #01-089-2642) and $NbTe_2$ (JCPDS #00-021-0605), respectively. Thus, it was confirmed that in situ phase segregation is possible after applying a rapid solidification process. For the samples doped with small fractions ($x \leq 0.01$), no secondary phase was observed. However, it can be expected that the same phase segregation of $NiTe_2$, and $NbTe_2$ occurred while the amount of the segregations was too small to be detected by XRD. Figure 1e,f shows the lattice parameters calculated from the XRD patterns for $Bi_{0.5}Sb_{1.5}Te_3(NiTe_2)_x$ (x = 0, 0.003, and 0.01) and $Bi_{0.5}Sb_{1.5}Te_3(NbTe_2)_x$ (x = 0, 0.005, and 0.01) with no changes in lattice parameters.

Figure 2 represents a schematic of energy band diagrams at heterointerfaces formed between $Bi_{0.5}Sb_{1.5}Te_3$ and the secondary phases, based on the concept of carrier energy filtering [14,15]. The main concept, which involves a $Bi_{0.5}Sb_{1.5}Te_3$ matrix with the precipitates, is illustrated in Figure 2. Carrier transfer induces band bending away from the heterointerfaces between the BiSbTe matrix and precipitates. The work function, electron affinity, and bandgap data for $NiTe_2$, $NbTe_2$, and $Bi_{0.5}Sb_{1.5}Te_3$ are shown in Table 1. The electron affinity of $Bi_{0.5}Sb_{1.5}Te_3$ is 4.50 eV and the band gap is 0.2 eV [15]. The work functions of $NiTe_2$ and $NbTe_2$ are 4.44 eV and 4.62 eV, respectively [17,18]. Barrier potentials may form near the interface; the presence of the electrostatic potential causes energy-dependent scattering of carriers at the heterointerfaces for $NiTe_2$ and $NbTe_2$, with $Bi_{0.5}Sb_{1.5}Te_3$ forming potential barriers of approximately 0.26 and 0.08 eV, respectively, as depicted in Figure 2. When hole carriers pass near the surfaces of secondary phases, low energy carriers are scattered, inducing the carrier filtering effect [14,15]. However, the energy blocking effect near the interfaces between $NbTe_2$ would be smaller due to their low barrier height of 0.08 eV (Figure 2b).

Figure 3 shows the σ and S as a function of temperature of the samples after melt spinning with a small addition ($x \leq 0.01$). $Bi_{0.5}Sb_{1.5}Te_3$ exhibited an σ of 465 S/cm at room temperature. As shown in Figure 3a, no change in σ was observed for x = 0.003; however, the x = 0.01 showed an increased σ (~500 S/cm at room temperature). In Figure 3b, the S values, as a function of temperature, are shown, while there is no distinct change in the error range. However, as shown in inset of Figure 3b, the power factor (σS^2) was increased from 2.68 to 3.15 mW/mK^2 for x = 0.01 as both the σ and S increased. In Figure 3c, after the addition of a small amount of $NbTe_2$, there is no significant change in the σ. As in Figure 3d, the S shows no distinct change in error range by $NbTe_2$ addition. Therefore, power factors (σS^2) also show no increase with the addition of $NbTe_2$ at all compositions (inset of Figure 3d).

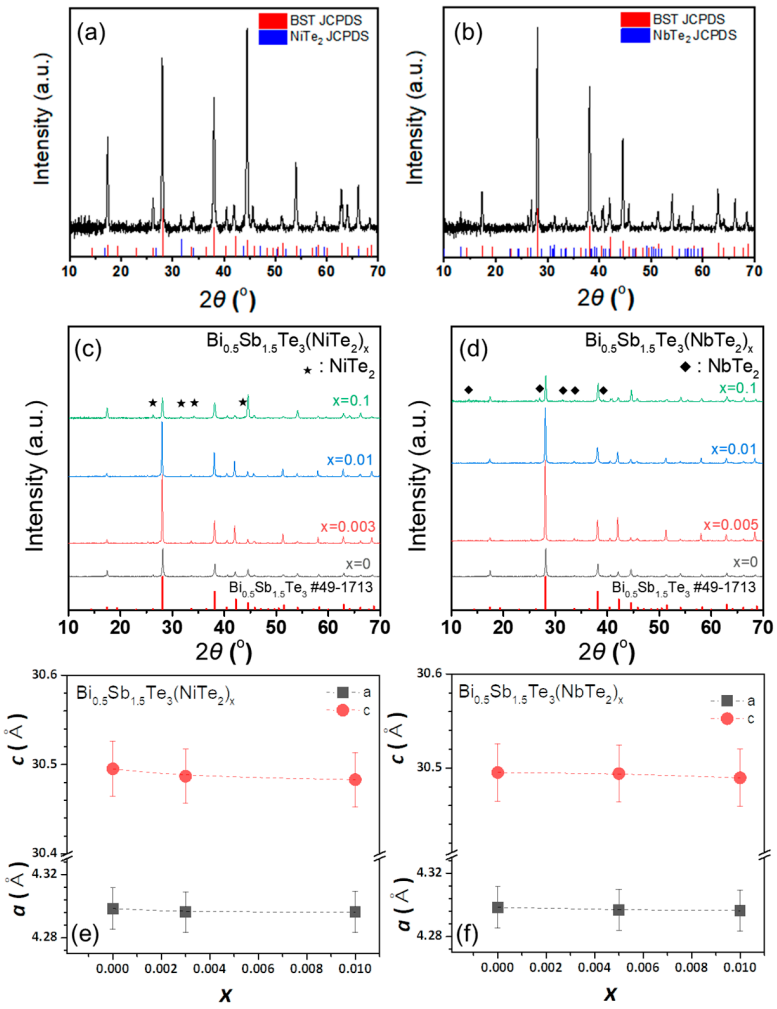


Figure 1. X-ray diffraction patterns for (**a**,**b**) melt-spun ribbons of (**a**) $Bi_{0.5}Sb_{1.5}Te_3(NiTe_2)_x$ (x = 0.1) and (**d**) $Bi_{0.5}Sb_{1.5}Te_3(NbTe_2)_x$ (x = 0.1)(**c**) and (**c**,**d**) SPS-sintered pellet of $Bi_{0.5}Sb_{1.5}Te_3(NiTe_2)_x$ (x = 0, 0.003, 0.01, and 0.1) and (**d**) $Bi_{0.5}Sb_{1.5}Te_3(NbTe_2)_x$ (x = 0, 0.005, 0.01, and 0.1). Lattice parameters calculated for (**e**) SPS-sintered $Bi_{0.5}Sb_{1.5}Te_3(NiTe_2)_x$ (x = 0, 0.003, and 0.01) samples and (**f**) $Bi_{0.5}Sb_{1.5}Te_3(NbTe_2)_x$ (x = 0, 0.005, and 0.01).

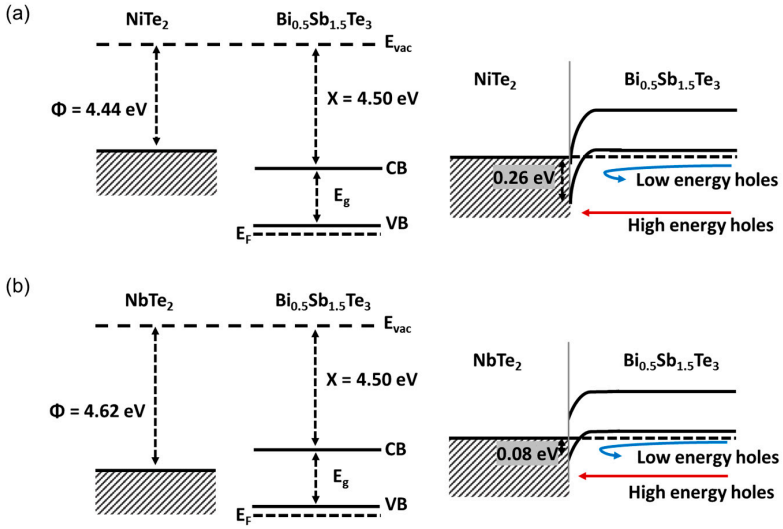


Figure 2. Schematic of energy band diagrams of the samples at the heterointerfaces between $Bi_{0.5}Sb_{1.5}Te_3$ and the secondary phase: (**a**) $NiTe_2$ and (**b**) $NbTe_2$.

Table 1. Work function (Φ) for $NbTe_2$ and $NiTe_2$, and electron affinity (χ) and band gap (E_g) for $(Bi_{0.5}Sb_{1.5})Te_3$.

Phase Segregation	Properties	Work Function (Φ) or Electron Affinity (χ) and Band Gap (E_g)
$NbTe_2$	Metallic	Φ = 4.62 eV
$NiTe_2$	Metallic	Φ = 4.44 eV
$(Bi_{0.5}Sb_{1.5})Te_3$	Semiconducting	E_g = 0.2 eV, χ = 4.50 eV

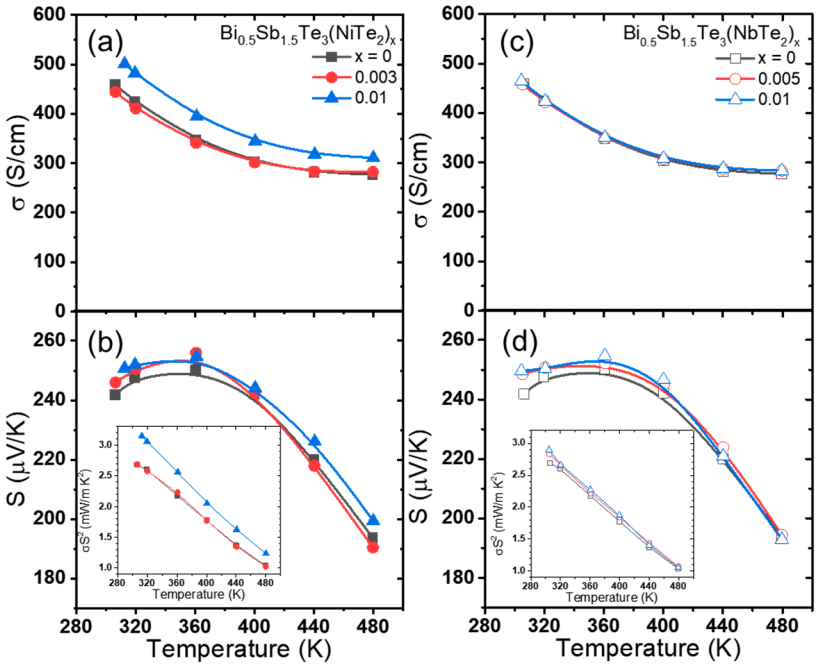


Figure 3. Temperature dependence of (**a**,**c**) the electrical conductivity and (**b**,**d**) the Seebeck coefficient for $Bi_{0.5}Sb_{1.5}Te_3(NiTe_2)_x$ (x = 0, 0.003, 0.01) and $Bi_{0.5}Sb_{1.5}Te_3(NbTe_2)_x$ (x = 0, 0.005, 0.01). Inset graphs in (**b**,**d**) exhibit the power factors of the samples.

Figure 4 shows the results from the Hall measurement (Hall carrier concentration, n_H, and Hall mobility, μ_H) and the Pisarenko plots at room temperature [14,15,19]. In Figure 4a, no clear relationship between n_H and μ_H is seen, while the n_H does not change for $NiTe_2$-added samples in the range of 9.5×10^{18}–9.6×10^{18} cm^{-3}. Figure 4b shows a Pisarenko plot (S as a function of n_H) with the effective mass m^* of 0.5 m_0, 0.55 m_0, and 0.6 m_0 shown as lines, based on Equation (1).

$$S = \frac{8\pi^2 k_B^2}{3eh^2}\left(\frac{\pi}{3n}\right)^{2/3} m^* T \quad (1)$$

where h is the Planck constant, k_B is the Boltzmann constant, e is the elemental electric charge and n is the carrier concentration. The gradual increase in m^* is clearly shown as x increased for $NiTe_2$-added samples (Figure 4b), although the noticeable decrease in n_H is not seen (Figure 4a). As n_H could vary for various reasons, the systematic increase in the m^* would suggest the presence of the carrier filtering effect due to the energy barrier of 0.26 eV (Figure 2a) as the density of interfaces between $NiTe_2$ and the matrix increases; for instance, the simultaneous increase in σ and S in $NiTe_2$-added samples (x = 0.01 compared to x = 0 of $Bi_{0.5}Sb_{1.5}Te_3(NiTe_2)_x$).

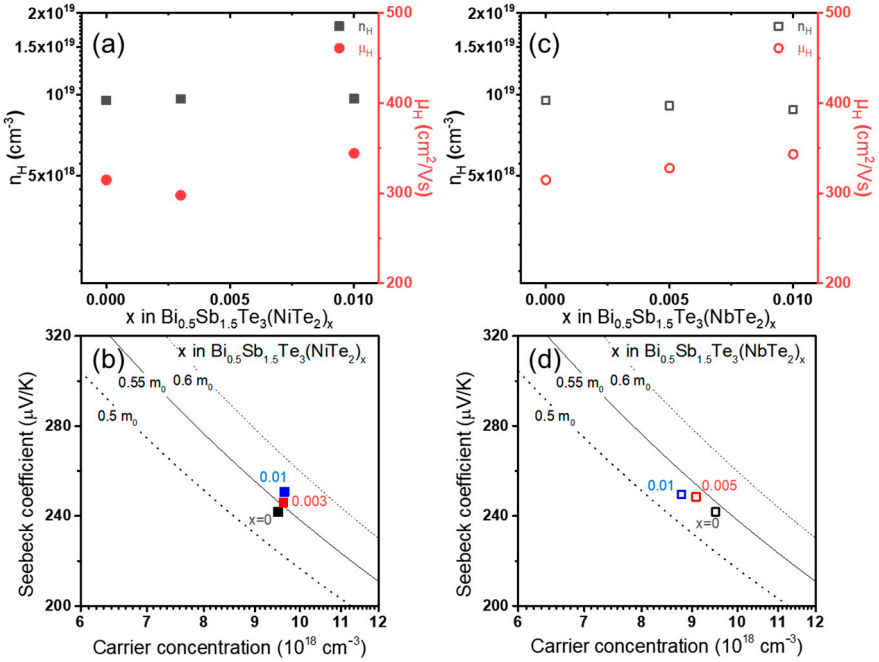


Figure 4. Carrier concentration and mobility for (**a**) $Bi_{0.5}Sb_{1.5}Te_3(NiTe_2)_x$ (x = 0, 0.003, 0.01) and (**c**) $Bi_{0.5}Sb_{1.5}Te_3(NbTe_2)_x$ (x = 0, 0.005, 0.01). Pisarenko plots (S as a function of carrier concentration) for (**b**) $Bi_{0.5}Sb_{1.5}Te_3(NiTe_2)_x$ (x = 0, 0.003, 0.01) and (**d**) $Bi_{0.5}Sb_{1.5}Te_3(NbTe_2)_x$ (x = 0, 0.005, 0.01) at room temperature.

Figure 4c shows that the n_H of $Bi_{0.5}Sb_{1.5}Te_3(NbTe_2)_x$ (x = 0, 0.005, 0.01) gradually decreased with x; the n_H values of 9.5 × 10^{18}, 9.0 × 10^{18}, and 8.7 × 10^{18} cm^{-3} for x = 0, 0.005, and 0.01, respectively. In contrast, the, μ_H increased gradually with increasing x, leading to values of 314, 327, and 343 cm^2/Vs for x = 0, 0.005, and 0.01, respectively. However, no change in m^* was shown. It seems that there is less carrier filtering influence on these samples due to the smaller barrier height (Figure 2b).

Figure 5 shows the temperature dependent κ of all samples (the uncertainty of κ would be around ±3%), while the inset shows the lattice thermal conductivity (κ_{latt}), calculated by subtracting the electronic contribution (κ_{elec}) calculated by the Wiedemann–Frantz law ($\kappa_{elec} = L \cdot \sigma \cdot T$), where L is Lorenz number, which can be estimated with Equation (2) (where L is in 10^{-8} WΩK^{-2} and S in μV/K) [20],

$$L = 1.5 + exp\left(-\frac{|S|}{116}\right) \quad (2)$$

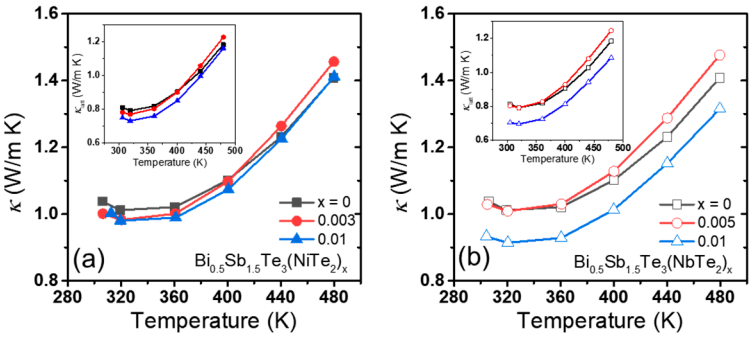


Figure 5. Thermal conductivity for (**a**) $Bi_{0.5}Sb_{1.5}Te_3(NiTe_2)_x$ (x = 0, 0.003, 0.01) and (**b**) $Bi_{0.5}Sb_{1.5}Te_3(NbTe_2)_x$ (x = 0, 0.005, 0.01). Insets shows the lattice thermal conductivity (κ_{latt}).

For $Bi_{0.5}Sb_{1.5}Te_3(NiTe_2)_x$ samples, a gradual decrease in κ_{latt} (0.81, 0.78, and 0.75 W/mK for x = 0, 0.003, and 0.01) was seen at room temperature (inset of Figure 5a), while there seems to be no distinct change in κ in Figure 5a. At high temperatures, the different influences from the bipolar conduction may affect the κ_{latt}. The second phases of $NiTe_2$ may scatter the phonons further to reduce room temperature κ_{latt}. For $Bi_{0.5}Sb_{1.5}Te_3(NbTe_2)_{0.01}$, the κ (and κ_{latt}) decreased to 0.92 W/mK (0.70 W/mK) at room temperature, compared to 1.03 W/mK (0.81 W/mK) of $Bi_{0.5}Sb_{1.5}Te_3$.

The estimated zT values of the samples are shown in Figure 6. For $Bi_{0.5}Sb_{1.5}Te_3(NiTe_2)_x$ samples (Figure 6a, the uncertainty of zT would be around ±17%), the zT was enhanced from 0.79 to 0.82 and 0.98 for x = 0.003 and 0.01, respectively, as the power factor increased due to increases in S, power factor, and m^* (Figures 3b and 4b). We speculate that the interface barrier height of 0.26 eV between $Bi_{0.5}Sb_{1.5}Te_3$ and $NiTe_2$ (Figure 2a) induced the carrier filtering effect, while there was slight systematic κ_{latt} reduction as well (inset of Figure 5a). For $Bi_{0.5}Sb_{1.5}Te_3(NbTe_2)_x$ samples (Figure 6b), with the much smaller barrier height of 0.08 eV between $Bi_{0.5}Sb_{1.5}Te_3$ and NbTe2 (Figure 2b), no increases in S, power factor, and m^* (Figures 3d and 4d) were seen. However, the reduction in κ_{latt} to 0.70 W/mK at room temperature (inset of Figure 5b) was achieved for x = 0.01. Therefore, the zT was also enhanced slightly from 0.79 to 0.83 and 0.94 for x = 0.005 and 0.01; however, this was mainly due to decreased κ (and κ_{latt}) for x = 0.01 (Figure 5b). For $Bi_{0.5}Sb_{1.5}Te_3(NiTe_2)_x$ samples, the improved electronic transport properties, caused by the possible carrier filtering effect, enhanced the zT, while the reduced thermal conductivity enhanced the zT in $Bi_{0.5}Sb_{1.5}Te_3(NbTe_2)_x$ samples.

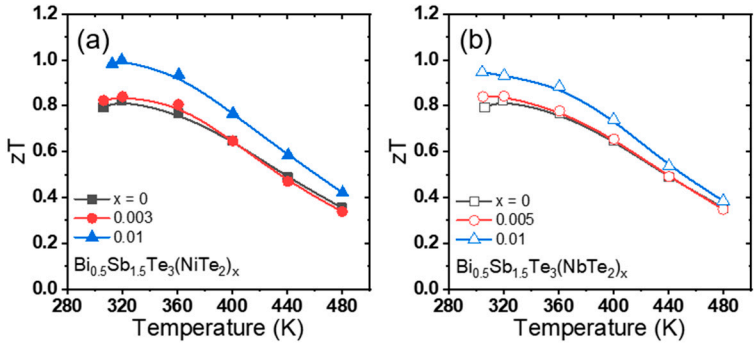


Figure 6. The zT values for (**a**) $Bi_{0.5}Sb_{1.5}Te_3(NiTe_2)_x$ (x = 0, 0.003, 0.01) and (**b**) $Bi_{0.5}Sb_{1.5}Te_3(NbTe_2)_x$ (x = 0, 0.005, 0.01).

4. Conclusions

The electrical and thermal transport properties of $Bi_{0.5}Sb_{1.5}Te_3$ with the formation of secondary phases of $NiTe_2$ and $NbTe_2$ were analyzed in regard to the carrier filtering effect. The possible carrier filtering effect was shown with enhanced Seebeck coefficient, power factor and effective mass for the $NiTe_2$ added samples, where the heterointerfaces are expected to form the energy barrier of 0.26 eV with the $Bi_{0.5}Sb_{1.5}Te_3$ matrix. However, for the $NbTe_2$ added samples with the energy barrier of 0.08 eV, only slight enhancement of the power factor was seen without increase in effective mass, implying that there is only minor influence of the carrier filtering effect. While the additional phonon scattering by the segregation was anticipated, the influence on κ was slight. Consequently, zT the zT was enhanced to 0.98 for $Bi_{0.5}Sb_{1.5}Te_3(NiTe_2)_{0.01}$ from 0.79 for $Bi_{0.5}Sb_{1.5}Te_3$ at room temperature, mainly due to the increases in S and m^* by the possible carrier filtering effect.

Author Contributions: Conceptualization, S.-i.K. and H.-S.K.; methodology, T.K.; formal analysis, J.A.; investigation, D.K., and J.H.J.; data curation, J.A.; writing—original draft preparation, S.-i.K.; writing—review and editing, H.-S.K. and T.K. All authors have read and agreed to the published version of the manuscript.

Funding: This work was supported by the Samsung Research Funding & Incubation Center of Samsung Electronics under Project Number SRFC-MA1701-05.

Institutional Review Board Statement: Not applicable.

Informed Consent Statement: Not applicable.

Data Availability Statement: Data available on request.

Conflicts of Interest: The authors declare no conflict of interest.

References

1. Stordeur, M. The Thermoelectric Figure of Merit in the Mixed Crystal System p-(Bi1−xSbx)2Te3. *Phys. Status Solidi B* **1990**, *161*, 831–835. [CrossRef]
2. Lee, K.H.; Kim, J.-Y.; Choi, S.-M. Recent Progress in Bi-Te-based Thermoelectric Materials. *J. Korean Ceram. Soc.* **2015**, *52*, 1. [CrossRef]
3. Snyder, G.J.; Toberer, E.S. Complex thermoelectric materials. *Nat. Mater.* **2008**, *7*, 105–114. [CrossRef] [PubMed]
4. Lee, K.H.; Kim, S.I.; Kim, H.S.; Kim, S.W. Band Convergence in Thermoelectric Materials: Theoretical Background and Consideration on Bi–Sb–Te Alloys. *ACS Appl. Energy Mater.* **2020**, *3*, 2214–2223. [CrossRef]
5. Paul, B.; Kumar, V.A.; Banerji, P. Embedded Ag-rich nanodots in PbTe: Enhancement of thermoelectric properties through energy filtering of the carriers. *J. Appl. Phys.* **2010**, *108*, 064322. [CrossRef]
6. Wu, L.; Li, X.; Wang, S.; Zhang, T.; Yang, J.; Zhang, W.; Chen, L.; Yang, J. Resonant level-induced high thermoelectric response in indium-doped GeTe. *NPG Asia Mater.* **2017**, *9*, e343. [CrossRef]
7. Toberer, E.S.; Baranowski, L.L.; Dames, C. Advances in Thermal Conductivity. *Annu. Rev. Mater. Res.* **2012**, *42*, 179–209. [CrossRef]
8. Mun, H.; Choi, S.-M.; Lee, K.H.; Kim, S.W. Boundary Engineering for the Thermoelectric Performance of Bulk Alloys Based on Bismuth Telluride. *ChemSusChem* **2015**, *8*, 2312–2326. [CrossRef] [PubMed]
9. Cho, H.J.; Kim, H.S.; Kim, M.; Lee, K.H.; Kim, S.W.; Kim, S.I. Enhanced Thermoelectric Performance of Cu-incorporated Bi0.5Sb1.5Te3 by Melt Spinning and Spark Plasma Sintering. *J. Electron. Mater.* **2020**, *49*, 2789–2793. [CrossRef]
10. Poudel, B.; Hao, Q.; Ma, Y.; Lan, Y.; Minnich, A.; Yu, B.; Yan, X.; Wang, D.; Muto, A.; Vashaee, D.; et al. High-thermoelectric performance of nanostructured bismuth antimony telluride bulk alloys. *Science* **2008**, *320*, 634–638. [CrossRef] [PubMed]
11. Kim, S.I.; Lee, K.H.; Mun, H.A.; Kim, H.S.; Hwang, S.W.; Roh, J.W.; Yang, D.J.; Shin, W.H.; Li, X.S.; Lee, Y.H.; et al. Dense dislocation arrays embedded in grain boundaries for high-performance bulk thermoelectrics. *Science* **2015**, *348*, 109–114. [CrossRef] [PubMed]
12. Kim, K.; Kim, G.; Kim, S.I.; Lee, K.H.; Lee, W. Clarification of electronic and thermal transport properties of Pb-, Ag-, and Cu-doped p-type $Bi_{0.52}Sb_{1.48}Te_3$. *J. Alloys Compd.* **2019**, *772*, 593–602. [CrossRef]
13. Lee, K.H.; Kim, H.S.; Shin, W.H.; Kim, S.Y.; Lim, J.H.; Kim, S.W.; Kim, S.I. Nanoparticles in $Bi_{0.5}Sb_{1.5}Te_3$: A prerequisite defect structure to scatter the mid-wavelength phonons between Rayleigh and geometry scatterings. *Acta Mater.* **2020**, *185*, 2710278. [CrossRef]
14. Faleev, S.V.; Léonard, F. Theory of enhancement of thermoelectric properties of materials with nanoinclusions. *Phys. Rev. B* **2008**, *77*, 214304. [CrossRef]
15. Kim, S.I.; Kim, S.W.; Roh, J.W.; Ahn, K.; Yeon, D.H.; Lee, K.H. Experimental evidence of enhancement of thermoelectric properties in tellurium nanoparticle-embedded bismuth antimony telluride. *J. Mater. Res.* **2012**, *27*, 2449–2456. [CrossRef]
16. Gayner, C.; Amouyal, Y. Energy Filtering of Charge Carriers: Current Trends, Challenges, and Prospects for Thermoelectric Materials. *Adv. Funct. Mater.* **2019**, *30*, 1901789. [CrossRef]
17. Lebègue, S.; Björkman, T.; Klintenberg, M.; Nieminen, R.M.; Eriksson, O. Two-Dimensional Materials from Data Filtering and Ab Initio Calculations. *Phys. Rev. X* **2013**, *3*, 031002. [CrossRef]
18. Zhang, C.; Gong, C.; Min, K.A.; Liang, C.; Oh, Y.J.; Zhang, H.; Wang, W.; Hong, S.; Colombo, L.; Wallace, R.M.; et al. Systematic study of electronic structure and band alignment of monolayer transition metal dichalcogenides in Van der Waals heterostructures. *2D Mater.* **2017**, *4*, 015026. [CrossRef]
19. Ioffe, A.F. *Physics of Semiconductors*; Academic Press: New York, NY, USA, 1960.
20. Kim, H.-S.; Gibbs, Z.M.; Tang, Y.; Wang, H.; Snyder, G.J. Characterization of Lorenz number with Seebeck coefficient measurement. *APL Mater.* **2015**, *3*, 041506. [CrossRef]